Title

Visualization and measurement of capillary-driven blood flow using spectral domain optical coherence tomography

Permalink

https://escholarship.org/uc/item/8df5w8xj

Journal

Microfluidics and Nanofluidics, 13(2)

ISSN

1613-4982

Authors

Cito, Salvatore
Ahn, Yeh-Chan
Pallares, Jordi
et al.

Publication Date

2012-09-01

DOI

10.1007/s10404-012-0950-6

Copyright Information

Peer reviewed

Visualization and measurement of capillary-driven blood flow using spectral domain optical coherence tomography

Salvatore Cito,
Department of Mechanical Engineering, University Rovira i Virgili, Av. Països Catalans, 26, 43007 Tarragona, Spain; Department of Chemical Engineering, University Rovira i Virgili, Av. Països Catalans, 26, 43007 Tarragona, Spain

Yeh-Chan Ahn,
Department of Biomedical Engineering, Pukyong National University, 599-1 Daeyeon 3-Dong, Nam-Gu, Busan, South Korea

Jordi Pallares,
Department of Mechanical Engineering, University Rovira i Virgili, Av. Països Catalans, 26, 43007 Tarragona, Spain

Rodrigo Martinez Duarte,
Department of Mechanical and Aerospace Engineering, University of California, Irvine, USA

Zhongping Chen,
Department of Biomedical Engineering, Beckman Laser Institute, University of California, Irvine, USA; World Class University Program, Ulsan National Institute of Science and Technology, 100 Banyeon-Ri, Eonyang-Eup, Ulju, Ulsan, South Korea

Marc Madou, and
Department of Mechanical and Aerospace Engineering, University of California, Irvine, USA; World Class University Program, Ulsan National Institute of Science and Technology, 100 Banyeon-Ri, Eonyang-Eup, Ulju, Ulsan, South Korea

Ioanis Katakis
Department of Chemical Engineering, University Rovira i Virgili, Av. Països Catalans, 26, 43007 Tarragona, Spain

Abstract

Capillary-driven flow (CD-flow) in microchannels plays an important role in many microfluidic devices. These devices, the most popular being those based in lateral flow, are becoming increasingly used in health care and diagnostic applications. CD-flow can passively pump biological fluids as blood, serum or plasma, in microchannels and it can enhance the wall mass transfer by exploiting the convective effects of the flow behind the meniscus. The flow behind the meniscus has not been experimentally identified up to now because of the lack of high-resolution, non-invasive, cross-sectional imaging means. In this study, spectral-domain Doppler optical coherence tomography is used to visualize and measure the flow behind the meniscus in CD-flows of water and blood. Microchannels of polydimethylsiloxane and glass with different cross-sections are considered. The predictions of the flow behind the meniscus of numerical simulations using the power-law model for non-Newtonian fluids are in reasonable agreement with the measurements using blood as working fluid. The extension of the Lucas–Washburn equation to

non-Newtonian power-law fluids predicts well the velocity of the meniscus of the experiments using blood.

Keywords

Capillary-driven flow; Blood flow; Microchannel; Optical coherence tomography; Non-Newtonian fluid

1 Introduction

The growing need for low cost yet reliable and highly efficient microfluidics for different applications presents the academic and industrial communities with a formidable challenge. Although the use of pumps is the most common way to move a fluid in a channel, they are often bulky and expensive (Groden et al. 2001). Capillary-driven flow (CD-flow) represents a less expensive and simpler alternative to active pumping mechanisms (Ichikawa et al. 2004).

Nature has perfected the use of capillary-driven flows. Tear drainage in eyes, water drainage in trees and mass transport of bio-substances (i.e. protein or oxygen) through the porous membrane of physiological tissues of organs are all phenomena that include a meniscus at the front of a fluid plug. CD-flows have lately gained importance in health care applications. For example, a surface-tension-driven method is often utilized in handheld devices in point-of-care diagnostics to detect glucose concentration or other relevant biomarkers in tiny samples of bio-fluids such as blood, urine, and saliva (Ahammad et al. 2009). For example, Chen et al. (2006a) proposed and optimized a CD-flow micro-mixer with asymmetric staggered grooved cavities. Swickrath et al. (2009) demonstrated an efficient CD-flow micro-mixer where the meniscus accelerates and decelerates as it comes into contact with alternated hydrophilic and hydrophobic surfaces.

Out of all biological fluids, blood is perhaps the most used and probably the best fluid to determine the health of a patient (Kim et al. 2006). Unfortunately, the turbidity of blood represents a major obstacle for the flow measurement and visualization. Particle image velocimetry (PIV) is widely used to study transparent fluids like water or air (Adrian 2005). For turbid fluids, the X-ray PIV technique (Kim et al. 2006) provides high spatial resolution even when working with opaque conduits. However, the imaging speed is slow and it needs synchrotron radiation (Ahn et al. 2008). There is currently no well accepted technique to study the CD-flow of blood behind the meniscus. Different techniques have been used by previous authors. Fåhraeus and Lindqvist (1931) used a Zeiss measuring microscope to show that a drop of blood flowing in a capillary tube has a higher concentration of corpuscles behind the meniscus than in the bulk. Kung et al. (2009) elucidated the effect that red cells have on the overall viscosity of blood and on the velocity of the meniscus using a CCD camera. Zhou and Sheng (1990) established the correlation between the macroscopic velocity of the meniscus and the microscopic parameters like contact line and frictional forces using a theoretical approach by solving numerically a mathematical model for immiscible fluid displacement. Recently, Kim et al. (2010) measured the blood flow in a microchannel using PIV with a confocal laser-scanning microscope. Nevertheless, this technique has a maximum recording velocity of 30 frames per second, which makes this technique slow for capturing the flow field behind the meniscus of a relatively fast CD-flow in a microchannel.

In this paper, we use spectral-domain Doppler optical coherence tomography (SDDOCT) to visualize and measure the flow behind the meniscus of blood and water. The technique is

based on the Doppler effect and low-coherence interferometry (LCI). SDDOCT allows a faster imaging speed and a higher sensitivity (de Boer et al. 2003; Choma et al. 2003; Leitgeb et al. 2003) than time-domain DOCT (Chen et al. 1997a, b; Izatt et al. 1997). These attributes help to overcome motion artifacts, increase maximum measureable velocity and decrease the minimum measurable velocity, which facilitate the study of turbid flows like blood. Ahn et al. (2008) have demonstrated the advantage of SDDOCT by measuring secondary flows of two fluids flowing in a meandering microchannel. On the other hand, LCI takes advantage of light with a short coherence length, which lets the user to define a depth window inside a sample where Doppler frequency is analyzed. By adjusting the path length of the reference arm of the Michelson interferometer on which optical coherence tomography is based, one can move the depth window to scan the information along the sample depth (axial-sections). A cross-sectional tomography is obtained by laterally combining a series of axial-sections (cross-sections). Finally, a volume image is constructed by scanning the sample beam to the third dimension and stacking a series of the cross-sectional tomographs. More details about this technique can be found in Ahn et al. (2008).

SDDOCT and standard video analysis are used in this study to visualize CD-flows of water and blood in microchannels. Special attention is placed on the visualization and measurement with SDDOCT of the flow close to the meniscus because of the potential effect of this flow on wall mass transfer rates. Results of numerical simulations of the flow behind the meniscus are compared with measurements. Measurements of the averaged velocity of the meniscus using a standard video analysis have been performed and they are compared with the predictions of the Lucas–Washburn equation for power-law non-Newtonian fluids.

2 Theory

When a blood droplet comes in contact with a hydrophilic microchannel (see Fig. 1) the surface tension draws the fluid into the microchannel and sets the blood into motion. At the line of intersection of the blood–air interface and the wall of the microchannel, the surface tension forces originating establish a meniscus with a certain contact angle. The dynamics of CD-flow in microchannels is defined mainly by the equilibrium between the surface tension and the viscous forces. However, it is not straightforward to determine the surface tension forces and the contact angle in a situation where the contact line is moving together with the meniscus. The contact angle evolves dynamically due to the interaction between the surface tension forces and the meniscus velocity. Pioneering attempts to understand the surface-tension-driven flows for practical applications were made by Washburn (1921). By assuming a steady-state flow and a balance between the viscous force and the pressure difference generated by the meniscus, this author obtained an equation, known as the Lucas–Washburn equation, that gives the position of the meniscus L as a function of the time t.

$$L(t) = \sqrt{\frac{R\sigma t \cos(\theta)}{2\mu}} \quad (1)$$

where R is the radius of the microchannel, σ is the surface tension, μ is the viscosity of the fluid and θ is the contact angle between the fluid and the surface material of the microchannel.

Equation 1 assumes that the fluid is Newtonian with constant physical properties, the meniscus is assumed spherical with a constant radius of curvature and a constant contact angle and the flow is incompressible and laminar (Washburn 1921). The velocity of the meniscus is

$$V_m = \frac{dL}{dt} = \sqrt{\frac{R\sigma \cos(\theta)}{8\mu t}} \quad (2)$$

More recently Joos et al. (1989) and Van Remoortere and Joos (1991) demonstrated the effect of the dynamic contact angle in the velocity of the meniscus and extended the theoretical solution of Washburn–Lucas equation for Newtonian fluids. The flow of blood in microchannel with diameter smaller than 0.3 mm is characterized by the presence of Fåhraeus–Lindqvist effect (Fåhraeus and Lindqvist 1931). When this effect becomes important, the Newtonian assumption breaks down and the real shearthinning rheology of blood is more appropriate to describe hemodynamics in capillaries. The most commonly used non-Newtonian mathematical models are namely, the, power-law, Casson (Chen et al. 2006b), and Carreau–Yasuda (Shibeshi and Collins 2005). It should be noted that the power-law model does not take into account the yield stress required to start moving the blood flow, consequently the following formulation is not valid for the first transient regime of CD-Flow, in which the meniscus start to move. The apparent viscosity for power-law fluids is modeled as

$$\eta = k \cdot \left(\dot{\gamma}\right)^{n-1} \quad (3)$$

The consistency index k and the power-law index n are dependent on the red blood cells distribution (Shibeshi and Collins 2005) and they have to be experimentally computed to take into account the Fåhraeus–Lindqvist effect. Blood is considered to be a shear-thinning fluid with $n < 1$ (Anand et al. 2005; Kim and Lee 2006; Taylor and Humphrey 2009). The magnitude of rate-of-strain tensor is defined as,

$$\dot{\gamma} = \sqrt{\frac{1}{2} \dot{\gamma}_{ij} \dot{\gamma}_{ji}} \quad (4)$$

where $\dot{\gamma}_{ij}$ is the rate-of-strain tensor and the viscous stress tensor is computed as,

$$\tau_{ij} = \eta \dot{\gamma}_{ij} \quad (5)$$

Blood at rest requires a yield stress to start flowing. The power-law does not take into account explicitly this characteristic feature. To introduce this effect into the non-Newtonian model the Casson or Carreau–Yasuda formulation should be considered (Shibeshi and Collins 2005). Nevertheless, the mathematical formulation of these last two models is not as simple as the power-law mathematical formulation model, which can be easily adapted to derive a simple non-Newtonian equation for the velocity of the meniscus.

A generalization of the Lucas–Washburn equation for power-law non-Newtonian fluids is derived in what follows to check its applicability to CD-flow of blood. The Lucas–Washburn equation assuming that the fluid is non-Newtonian and that the viscosity is given by Eq. 3 can be written as,

$$L(t) = R\left[\left(\frac{n+1}{3n+1}\right)\left(\frac{\sigma \cos(\theta)}{Rk}\right)^{\frac{1}{n}} t\right]^{\frac{n}{n+1}} \quad (6)$$

Note that if $n = 1$ in Eq. 5 (i.e. Newtonian fluid), Eq. 1 is recovered with $k \equiv \mu$.

Correspondingly, the velocity of the meniscus is,

$$V_m = \frac{dL}{dt} = \frac{n}{n+1} \frac{R\left[\left(\frac{n+1}{3n+1}\right)\left(\frac{\sigma \cos(\theta)}{Rk}\right)^{\frac{1}{n}}\right]^{\frac{n}{n+1}}}{\sqrt[n+1]{t}} \quad (7)$$

The L–W equation and the generalized L–W equations can be written in a non-dimensional form introducing the following parameters:

$$k = \gamma\mu; \beta = \frac{\mu}{\sigma}; T = \beta R; \quad x^* = \frac{x}{R}; t^* = \frac{t}{T}; v^* = \frac{1}{\beta} \quad (8)$$

Where γ is a consistency coefficient introduced to better quantify the non-Newtonian effect of blood in combination with n. γ together with n should be experimentally computed to implicitly take into account the Fåhraeus–Lindqvist effect. This can be used to define the non-dimensional L–W equations:

$$x^* = \sqrt{\frac{t^* \cos(\theta)}{2}} \quad (9)$$

and the non-dimensional generalized L–W equation

$$x^* = \left[\left(\frac{n+1}{3n+1}\right)\left(\frac{\cos(\theta)}{\gamma}\right)^{\frac{1}{n}}(\beta R)^{n^2-n} t^*\right]^{\frac{n}{n+1}} \quad (10)$$

3 Materials and methods

The microchannels used in this work were made out of glass or PDMS. The glass microchannels had circular cross-sections of different diameters between 200 and 500 μm and were acquired from VitroCom Inc. PDMS was acquired commercially as Sylgard® 184 base and curing agent. The PDMS microchannels have rectangular crosssection and were fabricated by casting the polymer on a master mold using the soft lithography technique (McDonald et al. 2000) as illustrated in Fig. 2. The master mold was fabricated by photo-patterning a 100 μm layer of SU-8 3050 (MicroChem Corporation, Newton, MA), a negative photoresist, on a silicon substrate. The PDMS polymer base and the curing agent are first mixed in a 10:1 ratio and immediately casted over the SU-8 mold. The whole assembly is placed inside a vacuum chamber for 1 h to degas the polymer before introducing it in a convection oven set at 65°C for further 4 h to complete the curing process. A total of eight microchannels are fabricated per batch. The microchannels are 5 cm long and have a rectangular cross-section $h = 100$ μm and $w = 500$ μm. Each microchannel connects two cylindrical chambers with $h = 100$ μm and 5 mm of diameter (see inset in Fig. 2b). Each individual channel is closed by bonding the PDMS piece to a common glass substrate and by pressing them together just after an exposure to oxygen plasma (200 W at 200 mTorr oxygen pressure) for 1 min. The closed channels are kept immersed in DI water until their use to preserve the hydrophilic property of the wall obtained during the treatment with plasma (Eddington et al. 2006).

PDMS was initially used to fabricate microchannels. However PDMS is a hydrophobic material and its surface has to be treated with oxygen plasma to become hydrophilic. After several trial experiments we observed that the phenomenological features of CD-Flow can be reproduced with PDMS microchannels. Nevertheless, after the surface treatment, the decay of the wettability of the PDMS surfaces was difficult to control and consequently it was not possible to perfectly reproduce quantitatively the flow features in PDMS microchannels in different experiments.

The experimental fluid samples include a 2.5% aqueous suspension of polystyrene beads with a diameter of 0.2 μm and a density of 1.05 g/cm^3 in DI water (Polysciences Inc., Warrington, PA) and bovine whole blood with EDTA as anticoagulant (Animal Technologies, Inc., Tyler, TX). Polystyrene beads in the water and red cells in bovine blood have been used as target particles to detect the Doppler effect during the SDDOCT scan while the fluids were flowing under CD-Flow. Since the density of polystyrene beads is very similar to that of water, the beads follow well the fluid velocity. The average distance between beads with a particle concentration of 2.5% is much smaller than the current imaging resolution. Hence, the resolution is not limited by the particle number density.

The schematic of a SDDOCT set-up is shown in Fig. 3. Low-coherence light with a wavelength centered around 1,310 nm (full width at half maximum is 95 nm) is coupled into the source arm of a fiber-based Michelson interferometer. The light that is backscattered from the reference and sample arms is guided into a spectrometer. Interference fringes are sampled by the spectrometer with a $1 \times 1,024$ InGaAs linear detector array at 7.7 kHz. The wavelength range on the array was 130 nm, corresponding to a spectral resolution of 0.13 nm and an imaging depth (from A to A' in Fig. 3) of 3.4 mm in air. The probe beam, with a 15 μm spot diameter at the focal point, is fixed at the centre of the microchannel. The coordinates XYZ are fixed to the capillary tube, being X the direction of the tube axis. And xyz are the coordinates fixed to the sample arm of the SDDOCT being y the direction of the line AA'. The velocity component along the line of sight (y-axis) is measured along time while the sample is flowing. The particles moving toward the positive (negative) y-direction produce red shift (blue shift) in Doppler frequency. SDDOCT measures the vertical-component of the velocity field, which is the particle velocity projected on the incident light. When the incident light is normal at the top or bottom surface of the microchannel, the detected velocity does not include the primary flow. Because high backscattering from the top and bottom surfaces may lead to saturation of the detector in the spectrometer the microchannel is slightly tilted with respect to the Z-axis by $a = 2°$ from the normal illumination (see Fig. 3). If the normal illumination has a relationship between two frames: $x = X$, $y = Y$, and $z = Z$, the new relationship due to the tilting is $z = Z$, $x = X\cos(a) + Y\sin(a)$, and $y = -X\sin(a) + Y\cos(a)$. Note that because of the tilting, the effect of the primary flow is included in the velocity component along the line of sight (y-axis) measured by SDDOCT. More details on the experimental set-up and the comparison of the SDDOCT technique with, for example, PIV and μPIV are reported in Ahn et al. (2008).

The glass microchannels with circular cross-section were adhered to a standard ruler to measure the time evolution of the position of the meniscus. A drop of blood was then deposited at the inlet. The sample was immediately drawn into the capillary by surface tension and its progress was recorded using a video camera at 29 frames per second. The frames of the video were processed to track the meniscus position. A similar experimental approach was proposed by Fan et al. (2001) to track the meniscus of standard engine oil flowing in a microchannel under surface tension forces.

The CD-flow has been simulated using the finite volume commercial code Fluent with second order accuracy. Figure 4 shows the two-dimensional physical model considered for

the simulations of the CD-flow in a large-aspect ration rectangular microchannel. The momentum equations have been solved in an inertial reference frame, which is moving at the same constant speed as that of the meniscus. Figure 4 indicates the boundary conditions with respect to this moving reference frame. It can be seen that the wall is moving at constant velocity and that a fully developed velocity profile is imposed at the inlet of the channel. The shear stress at the meniscus is considered to be zero and symmetry is considered with respect $y = 0$. In this study, the calculations have been performed with the power-law model for non-Newtonian fluids available in the code. Structured meshes with about 10^4 finite volumes are used, as indicated by initially carried out grid independence tests.

4 Results and discussion

4.1 Averaged axial velocity of CD-flow of blood

The CD-flow in circular microchannels with diameters of 200, 300, 400 and 500 μm was recorded using a video camera to determine the time evolution of the position of the meniscus and to check the validity of Eqs. 1 and 5 for CD-flow of blood. As an example, Fig. 5 shows the flow of blood in a circular microchannel of 300 μm of diameter at different times. The images of the video were post-processed to determine the position of the meniscus.

Figure 6a shows the measured position of the meniscus in comparison with the positions predicted using Eq. 9 for Newtonian fluids and Eq. 10 for power-law non-Newtonian fluids. The experimental data has been fitted with a nonlinear least square method. First, the fitting was applied to Eq. 9. For this equation, an optimum contact angle $\theta = 65°$ was computed for the microchannel with $D = 500$ μm and an optimum contact angle $\theta = 62°$ was computed for the microchannel with $D = 200$ μm. These values are in agreement with those reported by Chakraborty (2005). Then, the same fitting algorithm was applied to the Eq. 10 with contact angle of $\theta = 65°$, from this fitting four different values of n and α have been calculated (i.e. 1 for each microchannel diameter; $D = 200$, 300, 400 and 500 μm). The dependency of the values on R have been fitted respectively with second and third order polynomials (see Eqs. 11, 12).

$$\gamma = a \cdot R^2 + b \cdot R + c \quad (11)$$

$$n = d \cdot R^3 + e \cdot R^2 + f \cdot R + g \quad (12)$$

The values of the coefficients of the polynomials (Eqs. 11, 12) are: $a = 0.22$, $b = -0.519$, $c = 1.3048$, $d = 0.1909$, $e = -0.6496$, $f = 0.7377$, $g = 0.72$ if R is in μm. All the fittings have a correlation coefficient of r^2 0.99.

The measured averaged velocity and the predictions obtained with Eq. 9 and Eq. 10 are plotted in Fig. 6a for the largest (D = 500 μm) and the smallest (D = 200 μm) capillaries used. It can be seen in Fig. 6a that Eq. 10 for non-Newtonian fluids predicts much better the time-evolution of the position of the meniscus than Eq. 9, which is valid for Newtonian fluids. As shown in Fig. 6b, the measured averaged velocities of the meniscus are also better predicted if the non-Newtonian behavior of the blood is considered.

4.2 Visualization and measurement of the velocity field behind the meniscus of the CD-flow

An example of an image of a CD-flow of water in a glass microchannel obtained using SDDOCT technique is shown in Fig. 7a. The vertical axis corresponds to the Y direction, which is tilted 2° with respect to the radial direction of the microchannel, and the horizontal axis to the time, according to the fixed position of the probe (see Fig. 3). The colors correspond to the velocity component of the velocity vector parallel to the y-direction. Note that the color legend indicated in Fig. 7 is circular, so the abrupt changes from red to blue (or from blue to red) indicate absolute values of the vertical velocity component of about 2.5 mm/s. Figure 7b shows the contours of the radial velocity component predicted by the simulations. In this figure, some fluid particle paths that follow the velocity field viewed from a reference frame moving at the averaged velocity of the meniscus (see Fig. 4) have been included. It can be seen that the flow pattern near the meniscus of Fig. 7b corresponds to flow pattern near the meniscus of Fig. 7a, where the velocity vector points toward the top part of the wall of the microchannel.

Figure 8 shows an image of the flow behind the meniscus of a CD-flow of an aqueous suspension of polystyrene beads in a PDMS microchannel. The image indicate that the intensity of the vertical velocity component near the meniscus is different in the top half of the microchannel where the color is blue in comparison with the bottom half where the color is red and it changes abruptly to blue. This different intensity is produced by the different contact angle on the top glass wall and bottom PDMS wall of the channel, as described in Sect. 3.

The images of CD-flow of blood in circular glass microchannels are shown in Fig. 9. Blood exhibits strong light scattering behavior because of the difference of refractive indices between erythrocytes and plasma. In addition, there is a strong absorption of light by the hemoglobin. Consequently, the light penetration into the blood was limited to about 300 μm out of the 500 μm inner diameter of the channel and images of CD-flow of blood are restricted to the top part of the microchannel.

The images of Fig. 9 are depth (y) versus time plots at different axial positions X measured from the inlet of the microchannel (see Fig. 3). The positions are $X = 20$ mm (Fig. 9a), $X = 40$ mm (Fig. 9b), $X = 60$ mm (Fig. 9c) and $X = 80$ mm (Fig. 9d). The time history of the CD-flow of bovine blood was recorded three times for each position. The three measurements are plotted in the three rows of images shown in Fig. 9a–c. In Fig. 9d only two measurements with blood are shown in the two upper rows of images. For comparison purposes, the bottom row of images corresponds to CD-flow of water. The right columns of images in Fig 9a–d are zooms of the upper half regions of the corresponding images on the left column.

It can be seen in the images corresponding to blood of Fig. 9a–d that the intensity of the vertical velocity component decreases as the position of measurement is displaced downstream. Compare, for example, the images of Fig. 9a recorded at $X = 20$ mm with those of Fig. 9c taken at $X = 60$ mm. This is in agreement with the progressive reduction of the averaged axial velocity of the meniscus as it advances through the microchannel (see Fig. 6b). The comparison in Fig. 9d of the images of blood with those of water shows that the intensity of the vertical velocity component is larger in water than in blood. In fact the averaged velocity of the meniscus is about two times larger for water than for blood, according to the lower surface tension and the larger viscosity of blood with respect to the water ($\sigma_{blood}/\sigma_{water} \approx 0.75$, $\mu_{blood}/\mu_{water} \approx 3$).

The CD-flow far enough from the meniscus is a fully developed laminar flow with a radial velocity component equal to zero (see Fig. 7). In this situation the vertical profile of the axial velocity component can be determined from the Doppler shift, measured by the SDDOCT technique, considering that the microchannel is tilted 2°, as shown in Fig. 3. Figure 10 shows the measured axial velocity profiles of blood in circular glass microchannel at different times when the meniscus is far from the probe (i.e. at time 0.59, 1.23 and 2.08 s). Note that the origin of time, $t = 0$, corresponds to the instant when the meniscus reached the probe beam located at $X = 20$ mm.

The axial velocity profile of blood in a circular microchannel, assuming that it is a non-Newtonian power-law fluid, can be written as (Bird et al. 1997),

$$u = V_m \left(\frac{3n+1}{n+1} \right) \left[1 - \left(\frac{r}{R} \right)^{\frac{n+1}{n}} \right] \quad (13)$$

where V_m is given by Eq. 7. The theoretical velocity profiles indicated in Eq. 13 and calculated using the optimum θ and the coeficients n and γ computed with Eqs. 11 and 12, have also been plotted in Fig. 10. It can be seen that the use of Eqs. 8 and 7 to predict the time evolution of the axial velocity profile of CD-flow of blood is in agreement with the measurements given the scatter of the experimental data. According to Eq. 7, at $X = 20$ mm the averaged meniscus velocity at $t = 0$, 0.59, 1.23 and 2.08 s are, respectively, 23.18, 14.37, 11.3 and 8.99 mm/s. The plot of the experimental data in Fig. 10 has been smoothed using a weighted linear least squares 1st degree polynomial to implement a local regression to the experimental data. Furthermore, this smoother assigns lower weight to outliers in the regression and assigns zero weight to data outside six mean absolute deviations. The experimental data of Fig. 10 have a standard deviation $s = 0.14$ with respect to the theoretical prediction. The quantitative comparison of the measurements of the vertical velocity component of the CD-flow of blood with the corresponding numerical predictions is shown in Fig. 11. Note that as indicated in Sect. 3 and in Fig. 3 the experimental technique allows the measurement of the velocity component parallel to the y-direction, which is tilted 2° with respect to the radial direction. The inset in Fig. 11 shows the image obtained with the SDDOCT technique and the numerically predicted contours of the velocity component parallel to the y-direction. This component has been computed using the axial, V_X, and radial, V_Y, components of the velocity vector obtained in the simulation [i.e. $v_y = V_Y \cos(2°) + V_X \sin(2°)$]. It can be seen that the numerical predictions agree with the measurements.

5 Conclusions

The capillary-driven flow of blood in glass and PDMS straight capillaries has been analyzed experimentally and numerically. The time-evolution of the position and the averaged velocity of the meniscus in glass microchannels have been measured. The corresponding predictions of the Lucas–Washburn equation assuming that blood behaves as a power-law non-Newtonian fluid are in agreement with the measurements. The SDDOCT technique has been used to measure the axial and vertical velocity profiles behind the meniscus. The measured profile of the axial velocity component is well reproduced by the closed solution of the fully developed flow of a power-law fluid in a circular with the averaged meniscus velocity predicted by the Lucas–Washburn equation for a power-law fluid. The measurements obtained using the SDDOCT technique confirmed the presence of the recirculation pattern predicted by the numerical simulations.

The successful application of the SDDOCT technique for the visualization and quantification of CD-Flow of blood encourage the use of this technique for the study of

hemodynamics in microsystems. Furthermore, the mathematical model validated in this work can be used for theoretical studies and it can open the perspective for a rational optimization of microfluidics devices mass transfer phenomena in CD-Flow. This has particular importance for the optimization of microfluidics devices which use CD-Flow of sample test (like blood but not only), as the pumping system. Examples of such microfluidics devices are the disposable test carriers like the test strip platform for blood glucose measurement or the immunochromatographic strip tests for disease like syphilis or gonorrhea (Haeberle and Zengerle 2007).

Acknowledgments

List of symbols

D	Diameter of the circular cross-section microchannel (m)
h	Height of rectangular cross-section microchannel (m)
k	Fluid consistency coefficient (see Eq. 3)
L	Length (m)
n	Flow behavior index
R	Radius of the microchannel (m)
t	Time (s)
u	Velocity component ($m\ s^{-1}$)
V	Velocity ($m\ s^{-1}$)
w	Width of the rectangular cross-section microchannel (m)
x, y, z, X, Y, Z	Cartesian coordinates (m)

Greek letters

α	Tilting angle
θ	Contact anglel
μ	Dynamic viscosity ($kg\ m^{-1}\ s^{-1}$)
ν	Kinematic viscosity ($m^2\ s^{-1}$)
η	Apparent viscosity ($kg\ m^{-1}\ s^{-1}$)
σ	Surface tension ($N\ m^{-1}$)
$\dot{\gamma}_{ij}$	Rate-of-strain tensor (s^{-1})
τ_{ij}	Viscous stress tensor ($N\ m^{-2}$)

Subindexes and superindexes

c   Circular

m   Meniscus

References

Adrian RJ. Twenty years of particle image velocimetry. Exp Fluids. 2005; 39:159–169.

Ahammad AJS, Lee JJ, Rahman MA. Electrochemical sensors based on carbon nanotubes. Sensors. 2009; 9:2289–2319. [PubMed: 22574013]

Ahn YC, Jung W, Chen Z. Optical sectioning for microfluidics: secondary flow and mixing in a meandering microchannel. Lab Chip. 2008; 8:125–133. [PubMed: 18094770]

Anand M, Rajagopal K, Rajagopal KR. A model for the formation and lysis of blood clots. Pathophysiol Haemost Thromb. 2005; 34:109–120. [PubMed: 16432312]

Bird, RB.; Armstrong, RC.; Hassager, O. Fluid mechanics. Vol. vol 1. Wiley; New York: 1997. Dynamics of polymeric liquids.

Chakraborty S. Dynamics of capillary flow of blood into a microfluidic channel. Lab Chip. 2005; 5:421–430. [PubMed: 15791340]

Chen Z, Milner TE, Dave D, Nelson JS. Optical Doppler tomographic imaging of fluid flow velocity in highly scattering media. Opt Lett. 1997a; 22:64–66. [PubMed: 18183104]

Chen Z, et al. Noninvasive imaging of in vivo blood flow velocity using optical Doppler tomography. Opt Lett. 1997b; 22:1119–1121. [PubMed: 18185770]

Chen CF, et al. A microfluidic nanoliter mixer with optimized grooved structures driven by capillary pumping. J Micromech Microeng. 2006a; 16:1358–1365.

Chen, Jie; Xi-Yun, Lu; Wang, Wen. Non-Newtonian effects of blood flow on hemodynamics in distal vascular graft anastomoses. J Biomech. 2006b; 39:1983–1995. [PubMed: 16055134]

Choma M, Sarunic M, Yang C, Izatt J. Sensitivity advantage of swept source and Fourier domain optical coherence tomography. Opt Express. 2003; 11:2183–2189. [PubMed: 19466106]

de Boer JF, et al. Improved signal-to-noise ratio in spectral-domain compared with time-domain optical coherence tomography. Opt Lett. 2003; 28:2067–2069. [PubMed: 14587817]

Eddington DT, Puccinelli JP, Beebe DJ. Thermal aging and reduced hydrophobic recovery of polydimethylsiloxane. Sens Actuators B Chem. 2006; 114:170–172.

Fåhraeus R, Lindqvist T. The viscosity of the blood in narrow capillary tubes. Am J Physiol. 1931; 96:562–568.

Fan H, Gao YX, Huang XY. Thermodynamics modeling for moving contact line in gas/liquid/solid system: capillary rise problem revisited. Phys Fluids. 2001; 13:1615.

Groden C, Laudan J, Gatchell S, Zeumer H. Three-dimensional pulsatile flow simulation before and after endovascular coil embolization of a terminal cerebral aneurysm. J Cereb Blood Flow Metab. 2001; 21:1464–1471. [PubMed: 11740208]

Haeberle S, Zengerle R. Microfluidic platforms for lab-on-a-chip applications. Lab Chip. 2007; 7(9): 1094–1110. [PubMed: 17713606]

Ichikawa N, Hosokawa K, Maeda R. Interface motion of capillary-driven flow in rectangular microchannel. J Colloid Interface Sci. 2004; 280:155–164. [PubMed: 15476786]

Izatt J, Kulkarni MD, Yazdanfar S, Barton JK, Welch AJ. In vivo bidirectional color Doppler flow imaging of picoliter blood volumes using optical coherence tomography. Opt Lett. 1997; 22:1439–1441. [PubMed: 18188263]

Joos J, Bracke M, Van Remoortere P. The kinetics of wetting in a capillary. J Colloids Interface Sci. 1989; 136:189–197.

Kim GB, Lee SJ. X-ray PIV measurements of blood flows without tracer particles. Exp Fluids. 2006; 41:195–200.

Kim DS, Lee SH, Ahn CH, Lee JY, Kwon TH. Disposable integrated microfluidic biochip for blood typing by plastic microinjection moulding. Lab Chip. 2006; 6:794–802. [PubMed: 16738733]

NIH-PA Author Manuscript   NIH-PA Author Manuscript   NIH-PA Author Manuscript

Kim WH, et al. Particle image velocimetry of the blood flow in a micro-channel using the confocal laser scanning microscope. J Optical Soc Korea. 2010; 14:42–48.

Kung CF, Chiu CF, Chen CF, Chang CC, Chu CC. Blood flow driven by surface tension in a microchannel. Microfluid Nanofluid. 2009; 6:693–697.

Leitgeb RA, Hitzenberger C, Fercher A. Performance of Fourier domain vs. time domain optical coherence tomography. Opt Express. 2003; 11:889–894. [PubMed: 19461802]

McDonald JC, et al. Fabrication of microfluidic systems in poly(dimethylsiloxane). Electrophoresis. 2000; 21:27–40. [PubMed: 10634468]

Shibeshi SS, Collins WE. The rheology of blood flow in a branched arterial system. Appl Rheolo. 2005; 15:398–417.

Swickrath MJ, Burns SD, Wnek GE. Modulating passive micromixing in 2-D microfluidic devices via discontinuities in surface energy. Sens Actuators B Chem. 2009; 140:656–662.

Taylor CA, Humphrey JD. Open problems in computational vascular biomechanics: hemodynamics and arterial wall mechanics. Comput Methods Appl Mech Eng. 2009; 198:3514–3523. [PubMed: 20161129]

Van Remoortere P, Joos P. The kinetics of wetting: the motion of a three phase contactline in a capillary. J Colloid Interface Sci. 1991; 141:348–359.

Washburn E. The dynamics of capillary flow. Phys Rev. 1921; 17:273–283.

Zhou MY, Sheng P. Dynamics of immiscible-fluid displacement in a capillary tube. Phys Rev Lett. 1990; 64:882–885. [PubMed: 10042105]
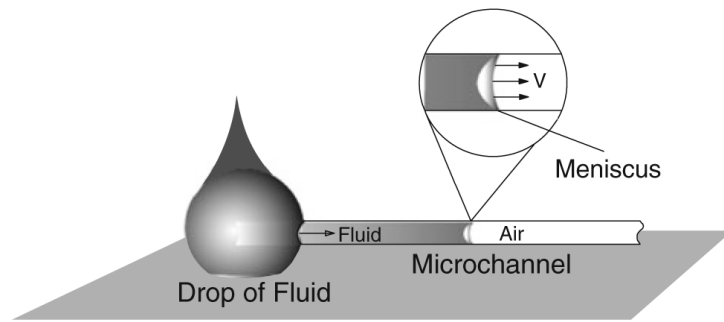
Fig. 1.
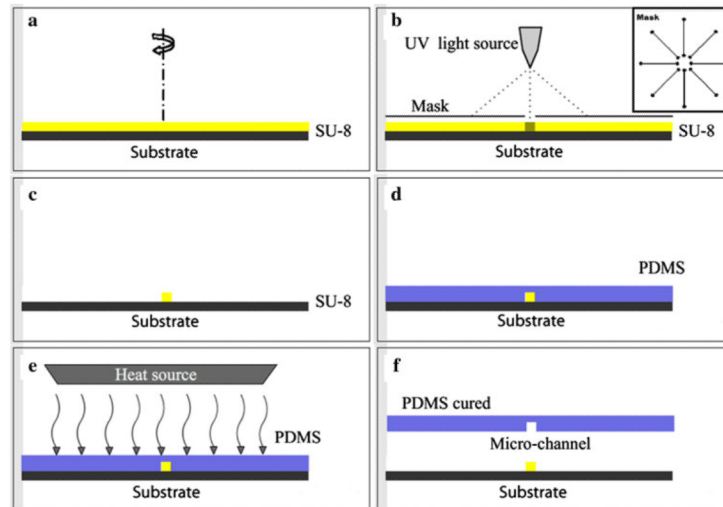Schematic of a microchannel drawing fluid from a droplet using capillary forces

Fig. 2.
Steps in the fabrication of microchannels using soft lithography of SU-8 and PDMS micro-molding. **a** Spinning of SU8 layer up to desired thickness, **b** SU8 crosslinking. The photo mask used is shown in the *inset*, **c** SU8 development, **d** PDMS casting, **e** PDMS crosslinking, **f** PDMS microchannel demolding
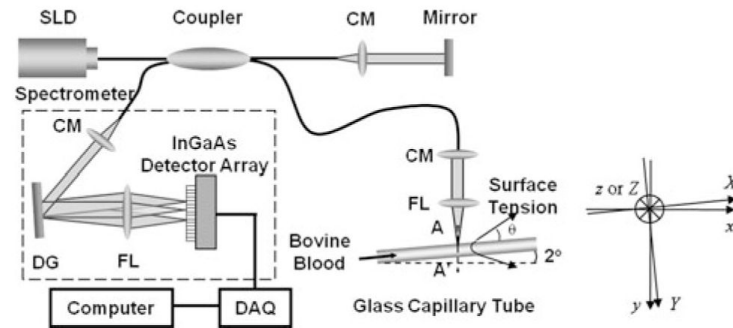
Fig. 3.
Experimental set-up for the spectral-domain Doppler optical coherence tomography technique. *SLD* super luminescent diode, *CM* collimator, *DG* diffraction grating, *FL* focusing lens. The coordinates *XYZ* are fixed to the capillary tube, being *X* the direction of the tube axis and *xyz* are the coordinates fixed to the sample arm of the SDDOCT being *y* the direction of the line AA'
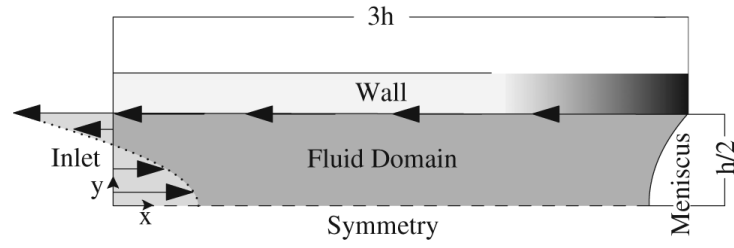
Fig. 4.
Physical model of the numerical simulations of the CD-flow in a high-aspect ratio rectangular microchannel
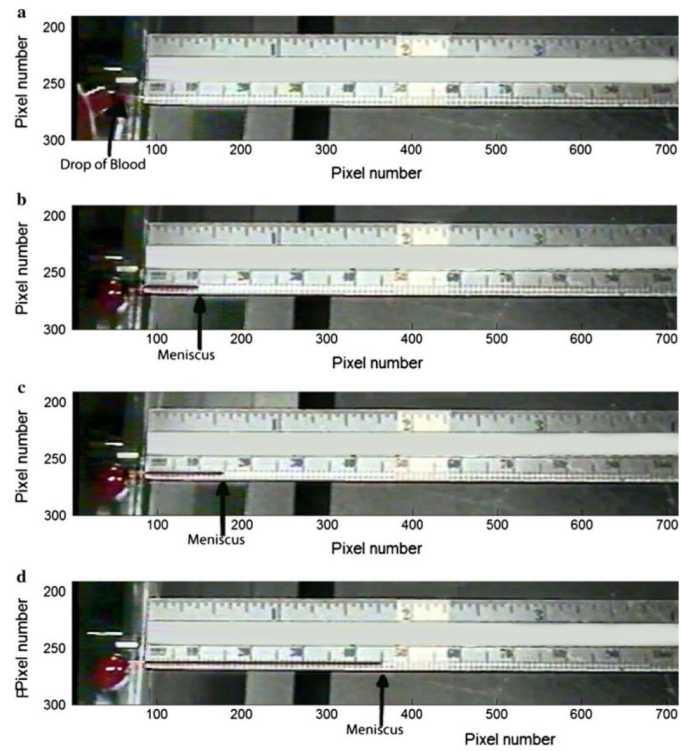
Fig. 5.
Video frames of bovine blood CD-flow in a glass microchannel with circular cross-section
and internal diameter of 300 µm CD-flow. **a** $t = 0$ s, **b** $t = 0.25$ s, **c** $t = 0.51$ s, **d** $t = 3.43$ s
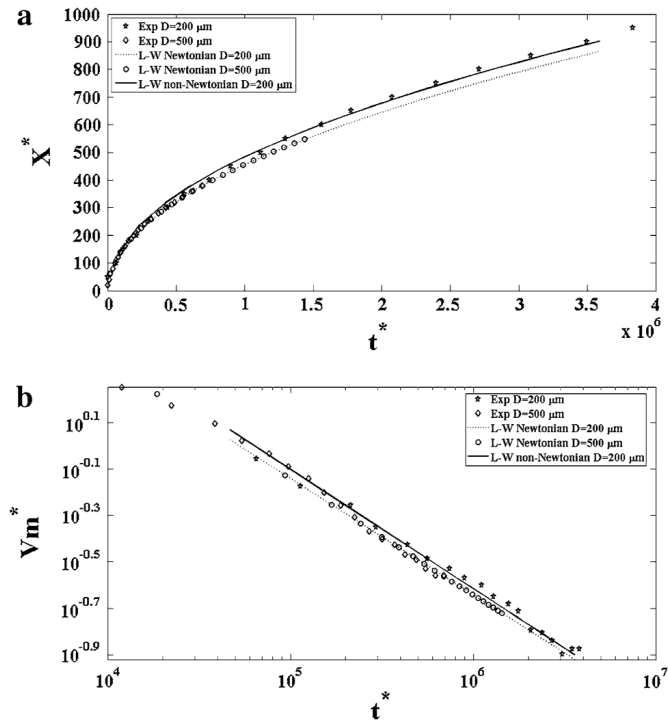
Fig. 6.
Measured and theoretically predicted time evolutions of the non-dimensional **a** position and **b** averaged velocity of the meniscus for the different microchannels (see Eqs. 9, 10)
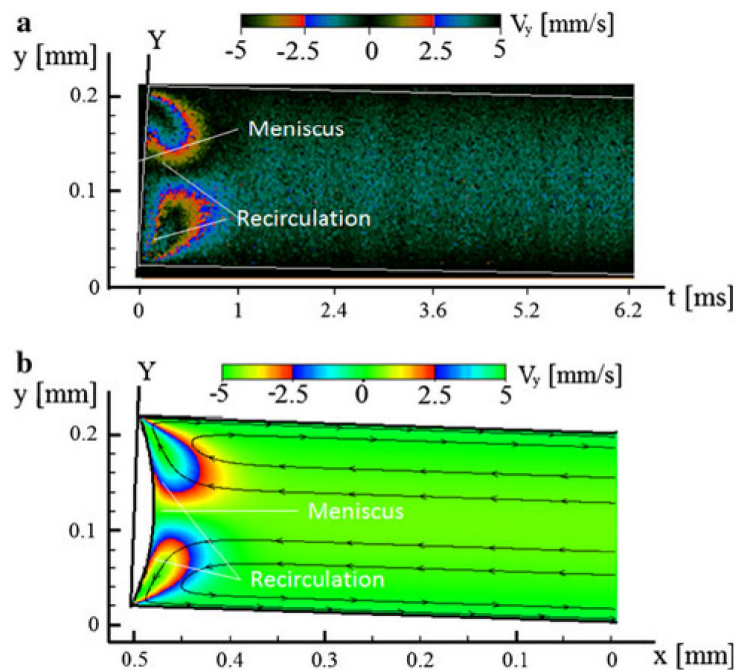
Fig. 7.
a Contours of the y-component of the velocity vector obtained with the spectral-domain Doppler optical coherence tomography of a CD-flow of an aqueous suspension of polystyrene beads in a glass microchannel with $D = 200\ \mu\text{m}$. **b** Contours of the y component of the velocity vector predicted by a numerical simulation of a CD-flow of water with $\theta = 70°$ in a microchannel with $D = 200\ \mu\text{m}$
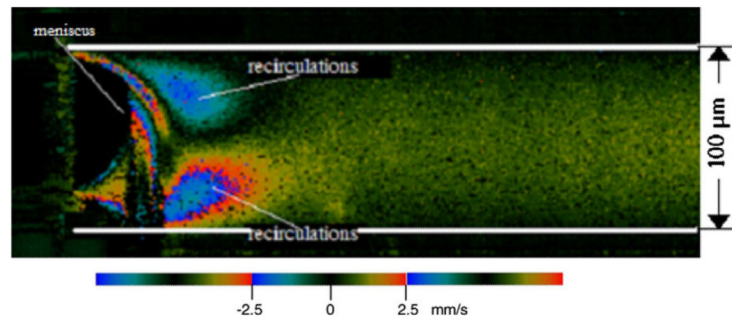
Fig. 8.
Image of the CD-flow obtained with the spectral-domain Doppler optical coherence tomography (SDDOCT). The fluid is an aqueous suspension of polystyrene beads in a PDMS microchannel
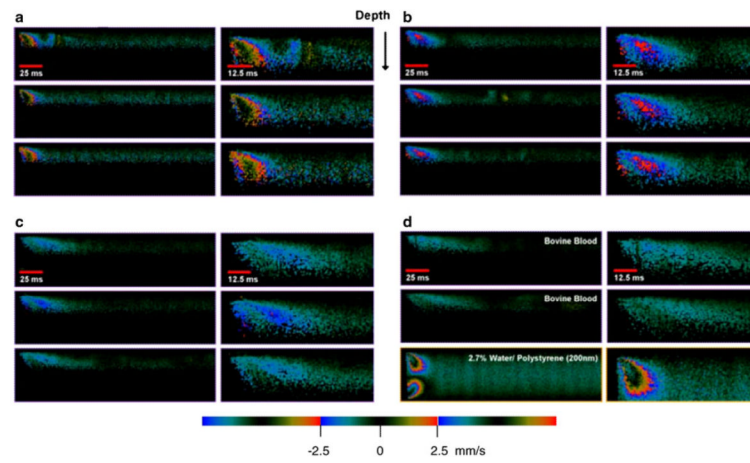
Fig. 9.
Images of the radial velocity component obtained by SDDOCT in a circular microchannel with an inner diameter of 500 µm. The images are depth (Y) versus time plots at different axial positions X measured from the inlet of the microchannel. **a** $X = 20$ mm, **b** $X = 40$ mm, **c** $X = 60$ mm, and **d** $X = 80$ mm
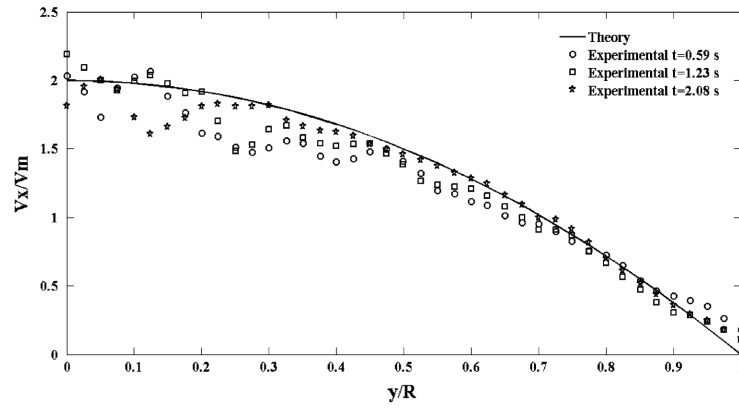
Fig. 10.
Axial velocity profile of blood flow measured at $X = 20$ mm at $t = 0.59$ s, $t = 1.23$ s and $t = 2.08$ s ($t = 0$ corresponds to the instant when the meniscus reached the probe beam located at $X = 20$ mm) in a circular microchannel with an inner diameter of 500 µm. The theoretical predictions given by Eq. 13 have been included. The normalized radius corresponds to r/R
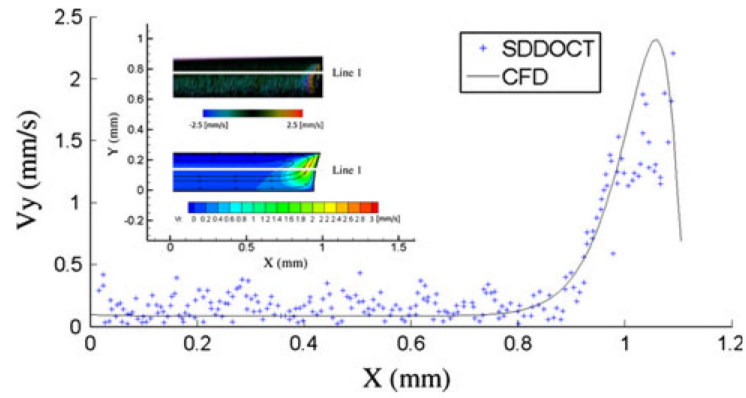
Fig. 11.
Comparison of the measured and numerically predicted radial velocity component in a CD-flow of blood in a circular microchannel with an inner diameter of 500 μm along *line 1*, indicated in the *inset*. The *inset* shows an image obtained by SDDOCT and the contours of the numerically predicted vertical velocity component. Some streamlines of the flow in the inertial reference frame moving at the velocity of the meniscus have been included